

Development Toward a Ground-Based Interferometric Phased Array for Radio Detection of High Energy Neutrinos

J. Avva^{a,b} K. Bechtol^{c,b} T. Chesebro^d L. Cremonisi^e C. Deaconu^b
A. Gupta^e A. Ludwig^{f,b} W. Messino^g C. Miki^h R. Nichol^e
E. Oberla^b A. Romero-Wolfⁱ D. Saltzberg^d C. Schlupf^d
N. Shipp^{j,b} G. Varner^h A. G. Vieregg^{f,k,b} S. A. Wissel^{l,d}

^aDept. of Physics, University of California Berkeley, Berkeley, CA 94720, USA

^bKavli Institute for Cosmological Physics, University of Chicago, Chicago, IL 60637, USA

^cWisconsin IceCube Particle Astrophysics Center, University of Wisconsin-Madison, Madison, WI 53703, USA

^dDept. of Physics and Astronomy, University of California Los Angeles, Los Angeles, CA 90095, USA

^eDept. of Physics and Astronomy, University College London, London, United Kingdom

^fDept. of Physics, University of Chicago, Chicago, IL 60637, USA

^gElectrical Engineering Dept., California Polytechnic State University, San Luis Obispo, CA 93407, USA

^hDept. of Physics and Astronomy, University of Hawaii, Manoa, HI 96822, USA

ⁱJet Propulsion Laboratory, California Institute of Technology, Pasadena, CA 91109, USA

^jDept. of Astronomy and Astrophysics, University of Chicago, Chicago, IL 60637, USA

^kEnrico Fermi Institute, University of Chicago, Chicago, IL 60637, USA

^lPhysics Dept., California Polytechnic State University, San Luis Obispo, CA 93407, USA

E-mail: avieregg@kicp.uchicago.edu, swissel@calpoly.edu

Abstract. A promising method for further measurements of high energy neutrinos at the PeV scale and above is through an in-ice radio interferometric phased array, designed to look for Askaryan emission from neutrinos interacting in large volumes of glacial ice. Such a detector would be sensitive to two populations of neutrinos: the PeV-scale astrophysical neutrino flux recently detected by IceCube, and the predicted cosmogenic ultra-high energy (UHE) flux ($E > 10^{17}$ eV). Characterizing these high energy neutrino populations is an important step toward understanding the most energetic cosmic accelerators, and the discovery of UHE neutrinos would allow us to probe fundamental physics at energy scales that are not achievable on Earth. We report here on studies validating the phased array technique, including measurements and a simulation of thermal noise correlations between nearby antennas, beamforming for impulsive signals, and a measurement of the expected improvement in trigger efficiency through the phased array technique. We also discuss the deployment of a system for characterization of the noise environment at Summit Station, a possible site for an interferometric phased array for radio detection of high energy neutrinos.

Contents

| | | |
|----------|--|-----------|
| 1 | Introduction | 1 |
| 2 | The In-Ice Interferometric Phased Array Concept | 2 |
| 3 | Thermal Noise Correlation Studies | 4 |
| 3.1 | Noise Correlation Measurements in an Anechoic Chamber | 4 |
| 3.1.1 | Measurement Setup | 4 |
| 3.1.2 | Antennas Used | 4 |
| 3.2 | Thermal Noise Simulation | 6 |
| 3.3 | Results | 6 |
| 4 | Validation of Beamforming Technique | 8 |
| 5 | Trigger Studies for Impulsive Events | 10 |
| 6 | Characterization of Summit Station: A Potential Site for an In-Ice Detector | 12 |
| 6.1 | System Design and 2015 Deployment | 13 |
| 6.2 | Noise Environment | 14 |
| 6.3 | Radio Attenuation Length of Ice at Summit Station | 16 |
| 6.4 | Firn Properties at Summit Station | 16 |
| 7 | Conclusions | 17 |

1 Introduction

In recent years, the IceCube experiment has detected a population of astrophysical neutrinos with energies up to ~ 10 PeV [1, 2]. The sources of these astrophysical neutrinos remain a mystery, their spectral index remains uncertain [3], and although there is no evidence for a spectral cutoff, the behavior at higher energies remains unknown [3].

In addition to the astrophysical population discovered by IceCube, there is a separate population of cosmogenic ultra-high energy (UHE) neutrinos ($E > 10^{17}$ eV) that awaits discovery. The detection of UHE neutrinos would open a new and unique window into the universe. A UHE neutrino observatory would enable the determination of the origin of the highest energy cosmic rays and the study of the evolution of the highest energy source populations. UHE neutrinos are made as a byproduct of the GZK process [4, 5], where cosmic rays with $E > 10^{19.5}$ eV per nucleon interact with the cosmic microwave background as they propagate through the universe within 50 Mpc of their source, going through a Δ^+ resonance, and yielding neutrinos as a result of the charged pion decay chain [6].

The twin science goals of following up on the IceCube measurement of astrophysical neutrinos at and above PeV energies, and discovering the highest energy cosmogenic neutrinos drives the design of developing and proposed experiments that aim to detect high energy neutrinos.

One promising method for detection of high energy neutrinos is via the Askaryan effect: the coherent, impulsive radio emission from electromagnetic showers induced by neutrinos

in a dielectric [7]. At long wavelengths (frequency less than a few GHz) the emission is coherent, so for high energy showers, the long-wavelength radio emission dominates. Beam test measurements have confirmed that the power in radio emission scales as the square of the energy of the shower at long wavelengths, demonstrating coherence [8–10]. A large volume of a dielectric material with a long radio attenuation length ($L_\alpha > 1$ km), such as glacial ice, is required to detect a significant rate of high energy astrophysical and cosmogenic neutrinos.

There are a variety of current and proposed experiments that search for Askaryan emission from high energy neutrino showers. The ANITA high altitude balloon experiment currently holds the best constraints on the flux of neutrinos above $10^{19.5}$ eV, and the proposed balloon-borne EVA experiment is a novel way to improve sensitivity at these highest energies [11, 12]. The ARA and ARIANNA experiments, ground-based radio arrays in early stages of development each with a small number of stations deployed in Antarctica, have energy thresholds $\gtrsim 50$ PeV, probing the heart of the cosmogenic neutrino regime [13, 14].

We discuss here developments toward an in-ice interferometric phased array detector. This type of radio detector allows us to push the energy threshold for radio detection down compared to currently-deployed and proposed experiments, further probing the astrophysical neutrino flux observed by IceCube while also increasing acceptance at higher energies. In Section 2, we review the in-ice interferometric phased array concept. In Section 3, we discuss measurements of thermal noise correlation between closely-spaced antennas, relevant for an interferometric phased array trigger. Section 4 details a validation of the beamforming technique for impulsive signals in an anechoic chamber. In Section 5, we discuss the implication of beamforming for a realistic triggering scheme. Section 6 reviews and details new measurements of the relevant characteristics of Summit Station, Greenland, including a characterization of the noise environment at Summit Station, the site where we performed an *in situ* test of a prototype detector. We conclude in Section 7.

2 The In-Ice Interferometric Phased Array Concept

The concept for an in-ice radio interferometric phased array for detection of high energy neutrinos was introduced in Reference [15]. In this Section, we summarize the concept and provide updated event rate estimates based on recent analyses from IceCube.

To reach the lowest possible energy threshold, the detector must be as close to the neutrino interactions as possible to minimize the effect of $1/r$ geometric propagation loss and exponential attenuation in the dielectric detection medium on electric field strength from a given neutrino event at the instrument. The lowest threshold will thus be achieved by a set of antennas that is embedded directly in a radio-transparent detection medium, such as glacial ice. This is the strategy employed by the ongoing ARA and ARIANNA experiments.

To achieve a low energy threshold and increase effective volume at higher energies, the detector must convert a given electric field strength at the location of the instrument into a high signal-to-noise (SNR) signal for the instrument to trigger on. High-gain antennas effectively increase the SNR of the observed signal for an incident electric field strength, but are directional – they are only sensitive to a subset of incident angles – and are physically impractical to deploy down narrow boreholes into the ice. If we instead combine signals from multiple low-gain antennas with the proper time delays to account for distances between antennas, we can effectively increase the gain of the system of antennas for incoming plane waves from a given direction. Incident plane wave signals such as neutrino signals add coherently, while thermal noise adds incoherently, increasing the SNR of the output signal for neutrino

events. Many different sets of delays of signals from the same antennas can create multiple effective antenna beam patterns that would together cover the same solid angle as each individual antenna but with much higher gain. The closer the antennas are physically, the fewer beams are needed to cover a given solid angle. This procedure is called beamforming. See Reference [15] for more details.

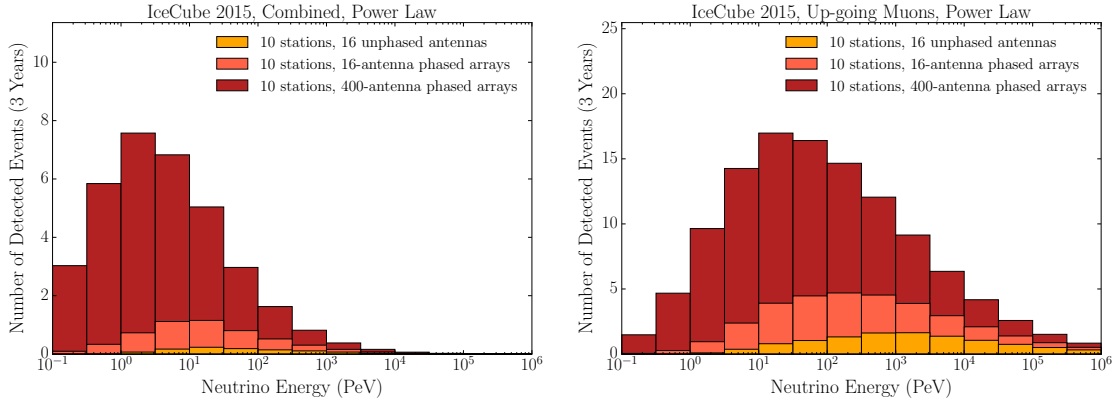


Figure 1. Triggered event rates vs. energy for three years of observation for 10 independent stations installed 100 m below the surface at Summit Station, Greenland. 16-antenna stations with no phasing are shown in yellow, 16-antenna stations with phasing are shown in orange, and stations with 400 phased antennas are shown in red. Event rates are based on two possible neutrino spectra based on the IceCube observed neutrino flux. The left panel uses an $E^{-2.5}$ power law, taken from the best-fit combined global IceCube analysis [3], and the right panel uses an $E^{-2.1}$ power law, taken from the IceCube up-going muon analysis [16].

| Station Configuration | Power Law ($E^{-2.5}$) | Power Law ($E^{-2.1}$) | Optimistic Cosmogenic | Pessimistic Cosmogenic |
|-----------------------|-----------------------------|-----------------------------|--------------------------|---------------------------|
| 16-antenna | 1.0 | 10.9 | 7.7 | 2.3 |
| 16-antenna, phased | 5.3 | 33.0 | 19.6 | 6.0 |
| 400-antenna, phased | 34.4 | 114.8 | 52.9 | 15.6 |

Table 1. Expectation values for the total number of triggered events in three years for 10 independent stations in different configurations for spectra based on recent IceCube analyses [3, 16] and for optimistic and pessimistic cosmogenic neutrino models [17].

Figure 1 shows results from a Monte Carlo simulation for an ideal detector, described in Reference [15]. Shown are triggered event rates vs. energy for two neutrino spectra, both consistent with recent analyses from IceCube, for a variety of trigger configurations for 10 independent stations located 100 m below the surface at Summit Station in Greenland. The results for 16-antenna stations are shown in yellow, 16-antenna stations with an interferometric phased array trigger are shown in orange, and 400-antenna stations with an interferometric phased array trigger are shown in red. The left-hand panel shows the best-fit spectrum ($E^{-2.5}$) from a combined global analysis of IceCube data [3]. The right-hand panel shows the best-fit spectrum ($E^{-2.1}$) from an analysis of up-going muon events, which is sensitive to a higher energy range and may be a better estimate of the spectrum at higher energies [16]. Table 1

shows the cumulative expected event rates over three years for a variety of models, including the two power law fits in Figure 1 and two cosmogenic neutrino models from Reference [17]. There is significant improvement, especially at low energies, by moving to an interferometric phased array trigger scheme. Moreover, complementary measurements made using the radio technique – especially with a phased array trigger – could further constrain the spectral index of the astrophysical neutrino flux.

3 Thermal Noise Correlation Studies

One of the underlying assumptions in the interferometric phased array simulation is that the thermal noise measured by each antenna in the array is uncorrelated with the thermal noise measured in its nearest neighboring antenna. The level at which thermal noise signals are correlated between antenna channels is one factor that determines the effective gain achieved by phasing together many antennas. In the limit of fully overlapping antennas, the thermal noise observed from the ice (~ 250 K) would be completely correlated, and the noise from the system would be completely uncorrelated (~ 75 K for the systems described in this paper). To determine how closely packed the antennas in a phased array can be without introducing a significant correlated noise contribution, we performed tests in an anechoic chamber and designed a simulation of thermal noise to compare to the measurements.

3.1 Noise Correlation Measurements in an Anechoic Chamber

3.1.1 Measurement Setup

We performed noise correlation measurements using a simple system in an anechoic chamber. Figure 2 shows a schematic diagram of the system setup, which consists of two antennas laid out end-to-end, with each antenna in its neighbor’s null. Signals from each antenna were amplified by a dual-stage front-end amplifier chain that included a 46 dB low-noise amplifier (MITEQ AFS4-00100200-10-15P-4) and a 40 dB amplifier (Mini-Circuits ZKL-1R5) separated by a 3 dB attenuator. DC power for the amplifiers was carried through the radio frequency (RF) cable, coupled by bias tees inside and outside the anechoic chamber. Signals were then filtered using a Mini-Circuits NHP 200 and NLP 450 or NLP 600, depending on the type of antenna used for the test. For all antenna types, which we discuss in Section 3.1.2, we used the NLP 600, except for the broadband dipole antennas that we developed, where we used an NLP 450. We used Times Microwave LMR-240 and LMR-400 cable, and cable lengths were identical in each signal chain. The noise temperature of each channel was ~ 75 K, dominated by noise from the front-end amplifier. Signals were then read out using a Tektronix MSO5204B oscilloscope, sampling at 5 GSa/sec. The walls of the anechoic chamber were between 1 m and 3 m from the antennas.

We changed the spacing between the antennas, ranging from as close as physically possible to a distance of over 1.5 meters between antenna feeds, to measure the level of correlated noise between channels as a function of the distance between the antennas.

3.1.2 Antennas Used

We used five different pairs of antennas for measurements in the anechoic chamber. We used two types of commercial antennas: folded dipole antennas from Telewave, Inc. (ANT275D and ANT400D) with bandpasses at 230-330 MHz and 360-450 MHz respectively^{1 2}. We also

¹<http://www.telewave.com/products/antennas/pdfs/TWDS-7048.pdf>

²<http://www.telewave.com/products/antennas/pdfs/TWDS-7079.pdf>

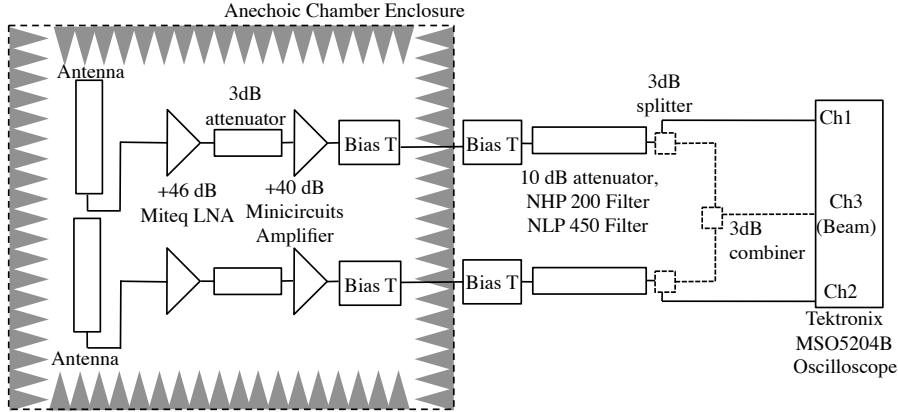


Figure 2. A schematic of the setup in the anechoic chamber for thermal noise correlation testing and validation of beamforming. For thermal noise correlation testing, there were no splitters or combiners before the oscilloscope. For validation of beamforming, described in Section 4, we added 3 dB splitters to each antenna channel and combined the signals to form a beam in hardware (shown with the dashed lines). We also set up a transmitter 4 m away inside the chamber for the measurements described in Section 4.

took data with two types of antennas that have been developed for the ARA experiment. The first is a broadband bicone antenna, used by ARA to detect vertically-polarized signals, and the second is a slot antenna that is sensitive to horizontal polarization when the antennas are deployed in boreholes [18]. The bicone antennas have a bandpass of 150-850 MHz and the slot antennas span 200-850 MHz.

Additionally, we took data with broadband dipole antennas that we developed, which we describe in detail here. Each antenna consists of two 20 cm copper cylinders, each with a diameter of 8 cm. The two sides of the antenna are connected at the feed with 0.64 cm copper rods. The antennas are read out via a 1.3 cm diameter Heliax cable. A 5.1 cm polyvinyl chloride collar separates the two halves of the antenna and provides strain relief at the feed. An antenna and the simulated design are shown in Figure 3a.

The antenna frequency range is optimized for Askaryan emission and the physical constraints of in-ice deployment in boreholes. The Askaryan signal is coherent up to about 1 GHz, but undergoes less propagation loss at low frequencies in glacial ice, so we preferred antennas in the 100-600 MHz range. The diameter of the dipoles was chosen to increase the bandwidth while ensuring that they would fit within reasonable sub-surface in-ice boreholes.

The antenna response, represented by the reflective S-parameter (S_{11}) in Figure 3b, reaches its first resonance at 262 MHz in air, which is reduced to 196 MHz when surrounded by glacial ice ($n = 1.78$). A simulation of the antenna response, constructed using HFSS³, is shown with a dashed line in Figure 3b. The higher-frequency dip corresponds to a second mode of the antenna. Simulations of the beam pattern in the antenna’s E-plane indicate that the beam pattern becomes slightly more directive with increasing frequency, rather than forming an additional null. The boresight gain is within 3 dB of its maximum of 2.9 dBi between 220 MHz and 755 MHz.

³<http://www.ansys.com/Products/Electronics/ANSYS-HFSS>

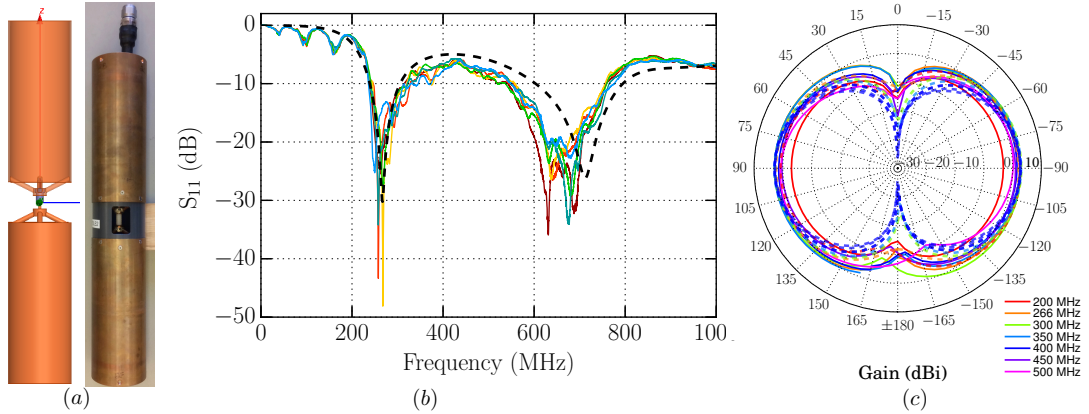


Figure 3. (a) A simulated (using HFSS, left) and constructed (right) broadband dipole. (b) The reflective S-parameter (S_{11}) for all the constructed antennas (colored, solid lines) compared with the HFSS simulation (dashed). (c) Radiation patterns (solid lines) compared with HFSS simulations (dashed lines).

3.2 Thermal Noise Simulation

Source of thermal noise are treated as oscillators each with an amplitude drawn from a Rayleigh distribution corresponding to a temperature of 300 K and a random phase drawn from a uniform distribution [19]. We create 10^5 of these oscillators, each with a frequency drawn from a uniform distribution over a 2 GHz bandwidth. The oscillators are thrown uniformly on a spherical shell that has a radius of 5 m and is centered on the point between two simulated antennas. We weight the amplitude of each oscillator by the sine of the incident angle on the antenna feed, where a zenith angle of zero corresponds to the location of the null of the antenna, to approximate a more realistic antenna beam pattern. We add the amplitude, modulated by the phase, for all generated oscillators in Fourier space for each antenna and filter the result using the magnitude of the frequency response of the filters we used in thermal noise correlation measurements (see Section 3.1). Uncorrelated noise is added to the simulated thermal noise for each channel that corresponds to the 75 K system temperature for each channel by generating noise with an amplitude drawn from a Rayleigh distribution and a random phase drawn from a uniform distribution over the same bandwidth as the thermal noise. We generate simulated noise traces at each antenna by inverse Fourier transforming the filtered spectra. By generating many sets of noise traces for antennas with different feed-to-feed spacings, we can make direct comparisons with measurements.

3.3 Results

We run identical analyses on simulated noise data sets and on noise correlation data taken in the anechoic chamber. Figure 4 shows the results of the noise correlation measurements for the ARA bicone antennas spaced as closely as physically possible (a feed-to-feed distance of 0.73 m), compared to measurements with the inputs to the front-end amplifiers terminated with a 50Ω load and results from the thermal noise simulation. The configuration with terminated amplifier inputs is used as a measure of the baseline level of correlated noise in the system between the two antenna channels.

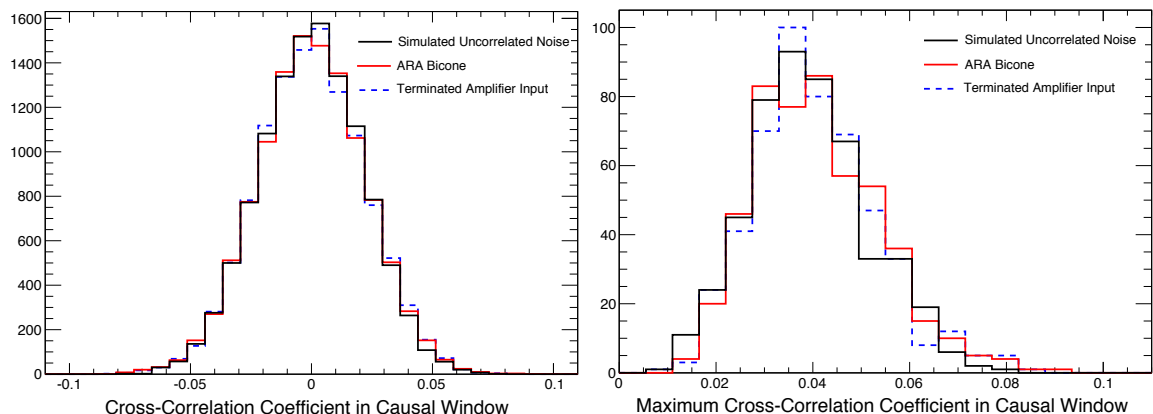


Figure 4. Left: a histogram of cross-correlation coefficient values between the two antenna channels over a time window ± 2.4 ns around zero time delay for each of ~ 500 recorded events compared to results from the simulation. This time window corresponds to possible time differences between antennas for incident plane wave signals from an arbitrary direction, determined by the spacing between the antenna feeds. Right: a histogram of the maximum of the absolute value of cross-correlation coefficient values between the two antenna channels in the causal time window for each of ~ 500 recorded events. The correlation values for a data set with the inputs to the front-end amplifiers terminated with a 50Ω load are shown in dashed red, and the values for the configuration with the ARA bicone antennas with their feeds separated by 0.73 m (the closest possible physical spacing) are shown in solid blue. The black line shows results from the thermal noise simulation for uncorrelated noise inputs.

The left-hand panel of Figure 4 is a histogram showing the cross-correlation coefficient between the two antenna channels over a causal time window (± 2.4 ns) for each of ~ 500 recorded events. We define the cross-correlation coefficient, \mathbf{C} , between two time-domain waveforms, $x(t)$ and $y(t)$, at a relative time delay τ between the waveforms, as

$$\mathbf{C}(x(t), y(t), \tau) = \frac{1}{N\sigma_x\sigma_y} \sum_{i=1}^N (x(t_i) - \bar{x})(y(t_i + \tau) - \bar{y}), \quad (3.1)$$

where N is the number of points in each waveform, σ_x and σ_y are the standard deviation of each waveform, and \bar{x} and \bar{y} are the mean of each waveform. The causal time window is determined by the feed-to-feed spacing between the antennas (0.73 m) and the speed of light.

The right-hand panel of Figure 4 is a histogram of the maximum of the absolute value of cross-correlation coefficient values shown in the left-hand plot for each recorded event. There is no significant correlation seen between the two channels when compared to the data taken with terminated amplifier inputs, even when the antennas were spaced as closely as physically possible. The correlation observed is consistent with simulated uncorrelated noise, shown by the black line in Figure 4.

We repeated this measurement with the antennas spaced farther apart and with a variety of types of antennas (Telewave ANT275D, Telewave ANT400D, and the ARA slot antennas), and all results are consistent with no observed correlation between adjacent antennas. We choose to show the results for the ARA bicone antennas because they are broadband across the full band of our system. Figure 5 shows the results of a comparison between the thermal noise simulation and data taken with the ARA bicone antennas at a variety of feed-to-feed

distances. For these antennas, the feeds are at the center of the antennas, and a spacing of zero in the simulation corresponds to fully overlapping antennas. Shown is the peak cross-correlation coefficient averaged over 500 simulated or measured events in a ± 6.0 ns time window, which is the causal window for the largest feed-to-feed spacing for which we made measurements (~ 2 m). We maintain a consistent time window in analysis and simulation at each distance to keep the trials factor the same across all distances shown. The error bars represent the standard deviation (RMS) of the peak cross-correlation coefficient values across the 500 events.

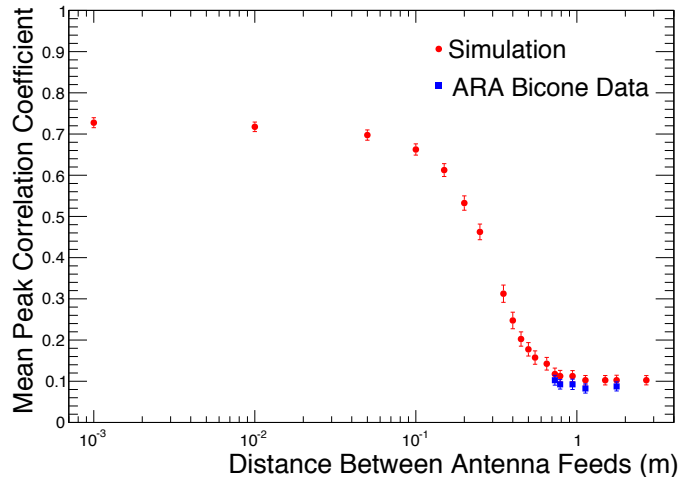


Figure 5. The peak cross-correlation coefficient averaged over 500 simulated or measured events in a ± 6.0 ns time window, which is the causal window for the largest feed-to-feed spacing for which we made measurements (~ 2 m). The error bars represent the standard deviation (RMS) of the peak cross-correlation coefficient values across the 500 events. The closest physically allowed feed-to-feed spacing is 0.73 m. Predictions from the simulation are shown in red and results from the measurements are shown in blue.

Significant noise correlation is not seen in simulation until the antennas are closer together than physically possible. At very small hypothetical feed-to-feed distances, the simulation approaches a correlation coefficient of 0.75, corresponding to the fraction of total noise in each channel from the 300 K thermal noise compared to the 75 K system temperature, which is independent between channels. At large spacings, the simulated data bottoms out at a peak correlation coefficient of 0.08, which would change with different allowed time windows. By the time the simulation reaches physically allowed spacings (> 0.73 m), we see a small deficit of noise correlation in measurements compared to simulation. We attribute this deficit at small physically allowed spacings to imperfect assumptions in the simulation, such as ignoring differences in antenna phase response as a function of angle, which would be a small effect but would serve to further decorrelate channels.

4 Validation of Beamforming Technique

We also performed a simple validation measurement of the beamforming technique in the anechoic chamber. We used a system configuration shown in the schematic in Figure 2. The

configuration was identical to the system described in Section 3, except for the following differences: after the second bias tee, we split the signal from each antenna channel and combined one branch of the signal from each channel to form a single beam that corresponds to zero time delay between the channels. This is a beam broadside to the antennas, at the highest-gain angle of each antenna. For this measurement, we used the broadband dipole antennas that we developed (see Section 3.1.2).

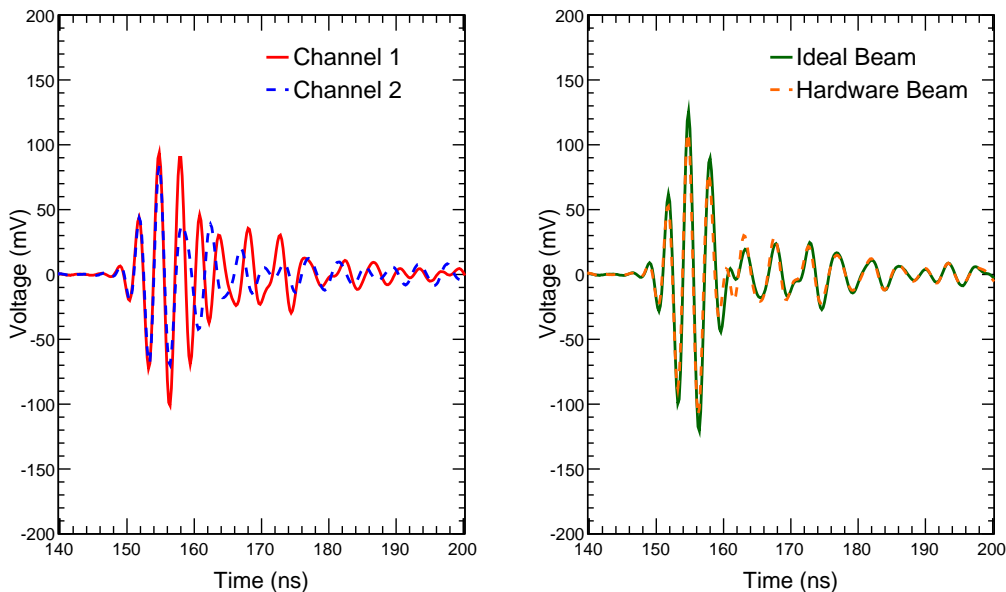


Figure 6. Left: an overlay of waveforms, averaged over 500 events, for Channels 1 and 2 in the system shown in Figure 2, when transmitting a fast impulse to the antennas. Right: an overlay of waveforms, averaged over 500 events, for the hardware-summed beam recorded in Channel 3 in the configuration shown in Figure 2 and the coherent waveform calculated directly from the averaged waveforms shown in the left-hand panel. This test uses the broadband dipole antennas described in 3.1.2.

We sent broadband, impulsive signals to the two receiving antennas from an identical transmitting antenna that was 4 m away inside the anechoic chamber, and was positioned broadside to the receivers for maximum transmission strength in the direction of the formed beam. The signals are generated using an Avtech AVP-AV-1S-C-P pulse generator, and are filtered before transmission with a Mini-Circuits NHP 200 and an NLP 450 filter.

Figure 6 shows the results of the measurement. The left-hand panel shows the impulsive signal received in the two independent antenna channels, averaged over 500 events recorded on the oscilloscope. Each channel had a slightly different impulse response, dominated by differences between individual antennas. Each channel also had a slightly different gain and noise temperature, dominated by differences in the individual front-end low-noise amplifiers. The right-hand panel shows the beam that we formed in hardware, compared to the ideal beam that should be formed, calculated in analysis. Some difference is evident between the beam formed in hardware and the ideal version formed in analysis, presumably due to the additional splitters and combiner added to the system. The peak-to-peak voltages agree to within 15%.

| | Noise V_{RMS} (mV) | Signal V_{pk2pk} (mV) | SNR (σ) |
|------------------------------|-----------------------------|--------------------------------|------------------|
| Antenna Channel 1 (measured) | 37.6 | 194.7 | 2.6 |
| Antenna Channel 2 (measured) | 28.5 | 154.3 | 2.7 |
| Hardware Beam (measured) | 35.5 | 217.2 | 3.1 |
| Ideal Beam (calculated) | 37.2 | 246.1 | 3.3 |

Table 2. A summary of the validation of the beamforming technique using data taken in an anechoic chamber. Shown are the noise levels, signal amplitude, and SNR of the signals measured for each antenna channel and the beam formed in hardware, as well as the properties of the expected ideal beam calculated using data from each antenna channel.

Before averaging together many waveforms to produce the high SNR waveform shown in Figure 6, we calculate the SNR of the signal that was received in each channel, including the hardware-formed beam, compared to the noise level in the system. We define SNR as half of the signal’s peak-to-peak voltage divided by the RMS of the noise ($\frac{V_{\text{pk2pk}}}{2\sigma}$). The results are shown in Table 2. We then calculate the ideal beam that should be formed and the noise level corresponding to superimposed noise from the individual antenna channels. Note that because of the differences between the two signal chains, we do not expect to see the $\sqrt{2}$ improvement in SNR that should be obtained for identical antennas and signal chains. The hardware beam matches the ideal beam well in terms of SNR, although both the signal level and noise level suffer slightly from additional losses introduced by the additional components in the signal chain.

5 Trigger Studies for Impulsive Events

We investigate the trigger rate and efficiency of a broadband phased array using the anechoic chamber measurements in combination with a simulation study of both noise and transient signals. A linear array of three Telewave ANT400D folded dipole antennas was placed in the anechoic chamber approximately 4 m from an ARA bicone antenna that was used as a transmitter (see Section 3.1.2). The Telewave antennas are mounted on a steel ground mast with a separation of 36 cm between the antenna phase centers and the ground mast. The antennas are spaced at a pitch of 55 cm. Each receiving antenna has the same signal chain as shown in Figure 2 and the signals are recorded at 5 GSa/sec.

We model the digital phasing and event triggering of a linear antenna array. The antenna channels are formed into beams by digitally delaying and coherently summing the individual antenna channels. A relative delay is applied between the digitized waveforms received at a pair of antennas, which corresponds to a beam angle, θ_n , of

$$n \Delta t = \frac{d}{c} \sin \theta_n, \quad (5.1)$$

where n is an integer, Δt is the sampling time interval, c is the speed of light in the medium, and d is the baseline between the pair of antennas. Many beams can be formed simultaneously to cover a wide angular range. For a fixed antenna spacing, the sampling rate sets the number of independent beams and the granularity of the angular coverage.

To detect transient events, a time-windowed power calculation is performed on each coherently summed beam, given by

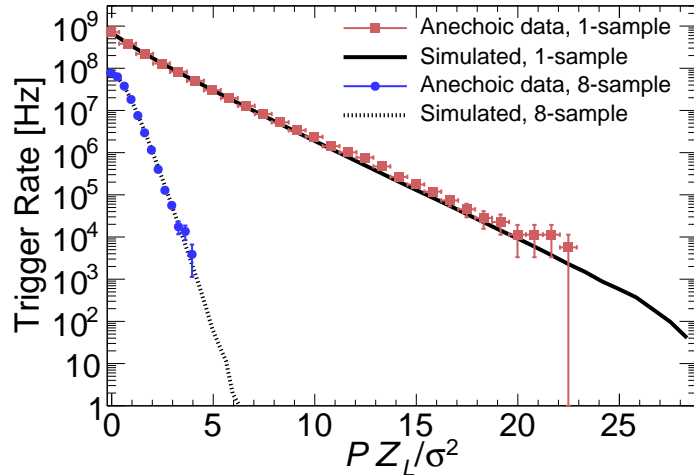


Figure 7. Trigger rate vs. normalized power threshold, PZ_L/σ^2 , for noise traces taken in the anechoic chamber using the three Telewave antennas (data points) compared to simulations of thermal noise (solid lines). Two trigger configurations are shown: the blue data points indicate the trigger rate when the average power is taken over a 9.6 ns window and incremented every 8 samples (4.8 ns). The red data points show the singles rate when the power is calculated at every sample point. We use the simulation to predict the threshold for rates lower than several kHz due to the limited amount of data taken in the anechoic chamber.

$$P_{window} = \frac{1}{N_s Z_L} \sum_{j=1}^{N_s} \left(\sum_{i=1}^{N_{ant}} V_{ij} \right)^2, \quad (5.2)$$

where N_s is the number of digitized samples in the time window, Z_L is the load impedance, N_{ant} is the number of antennas used in the beam, and V_{ij} is the digitized voltage at sample j within the time window for antenna i .

The relationship between the per-beam singles rate and trigger threshold is determined by N_s , as shown in Figure 7, where the power threshold, P , is normalized by the square of the noise RMS (σ^2) divided by Z_L . For these measurements, the data are down-sampled from 5 GSa/sec to 1.67 GSa/sec via decimation to reflect a Nyquist sampling rate for a system with a bandwidth of ~ 800 MHz. Two power calculations are shown: one in which the average power is calculated in a window of $N_s=16$ samples (9.6 ns) and sampled every $N_s/2=8$ samples (4.8 ns), and a second in which the power in each sample is recalculated at every sample point.

The optimal sampling interval for the power calculation is related to the dispersion of the signal going into the trigger. For the case in which the impulse response of the system is deconvolved before triggering it may be optimal to sample the power at every data sample because the signal power is contained in a short time interval. However, the system response is not unfolded from the signal in the baseline algorithm described here. A more efficient algorithm for the dispersive pulses recorded in the anechoic chamber calculates the power every 8 samples thereby including the majority of the power from a single transient pulse. With a power calculated from an 8-sample window, we find voltage thresholds, $\sqrt{PZ_L}$, of 2.34σ , 2.21σ , and 2.07σ , for noise singles rates of 10, 100, and 1000 Hz, respectively.

To measure the trigger efficiency, event rates were measured from the 3-antenna array

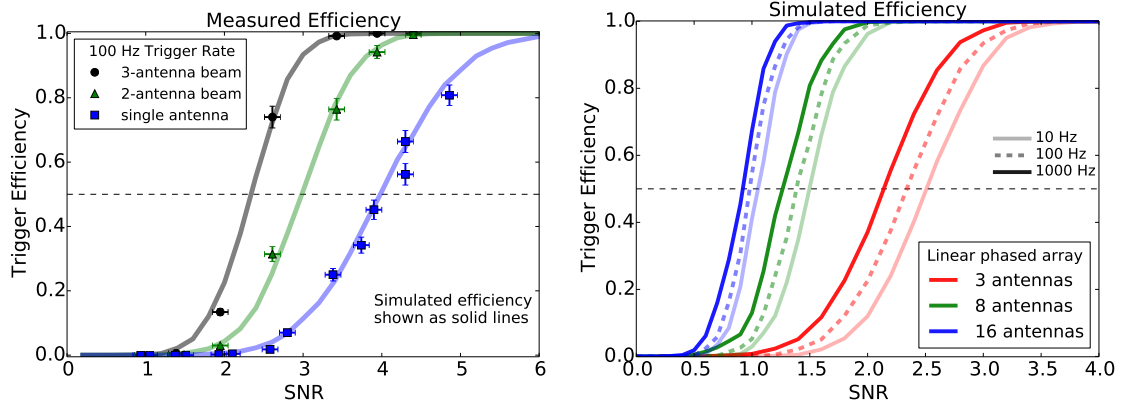


Figure 8. Trigger efficiency vs. SNR. The left plot shows anechoic chamber results from a 3-antenna array (data points) compared to a simulation of uncorrelated noise added to the system impulse response (lines). The data points are taken from anechoic chamber measurements with a fast impulsive signal and the average power was calculated at 8-sample intervals using a power threshold corresponding to a 100 Hz singles rate (dashed line from Figure 7). The right plot shows the simulated trigger efficiencies for 3, 8, and 16-antenna broadband phased arrays in a single formed beam. For each configuration, efficiency curves are drawn for per-beam trigger rates of 1 kHz, 100 Hz, and 10 Hz by the dark-solid, dashed, and light-solid line, respectively.

in the anechoic chamber while sending impulsive signals from the transmitting antenna at several attenuation levels. For each attenuation setting, we recorded 500 events. The SNR is defined as $\frac{V_{pk2pk}}{2\sigma}$ for a single antenna. The measured trigger efficiency at a trigger rate of 100 Hz, specified by Figure 7 using the 8-sample interval, is shown in the left plot in Figure 8. We choose 100 Hz as a baseline per-beam trigger rate, comparable to achieved trigger rates by currently-deployed experiments, such as ANITA. We measure the efficiency for a single antenna, the 0° beam formed by using 2 antennas, and the full 3-antenna 0° beam by comparing the power, calculated within the time window corresponding to the time when the pulse was transmitted using Equation 5.2, to the appropriate threshold level for the chosen trigger rate.

These measurements compare well with simulation results shown by the solid lines in the left-hand plot of Figure 8. The simulated curves include 5000 events in which the average impulse response of each antenna is added to the appropriate level of uncorrelated system noise (75 K for our system plus 300 K of room temperature thermal noise).

The simulation is extrapolated to larger phased arrays as shown on the right-hand plot in Figure 8, and curves are shown for each size array at 10, 100, and 1000 Hz per-beam trigger rates. The efficiency curves for the 8- and 16-antenna arrays assume equal impulse response for each antenna channel. A 16-antenna linear phased array that is set to trigger on impulsive events in a single beam at 100 Hz achieves a 50% efficiency at a SNR of about one. This is a significant improvement over single-antenna trigger thresholds, which reach 50% efficiency at an SNR of about four at the same trigger threshold.

6 Characterization of Summit Station: A Potential Site for an In-Ice Detector

We have also made measurements to characterize a potential site for deployment of an in-ice interferometric phased array: Summit Station in Greenland. Summit Station is a year-round

NSF operated site, located at N 72° 37' W 38° 28', near the highest point on the Greenland ice sheet. Summit Station sits atop 3 km of glacial ice, making it an ideal candidate site for radio detection of high energy neutrinos.

6.1 System Design and 2015 Deployment

An instrument was deployed at Summit Station in June 2015 to characterize the site and validate the phased array technique with an array deployed in the ice, as discussed in Reference [20]. The system used analog beamforming to combine signals from multiple antennas, as shown in the schematic of the RF signal chain in Figure 9. The system used the same front-end amplifier system described in Section 3.1.1. Each front-end amplifier was preceded by a 200 MHz high pass filter to protect the first stage amplifier from the 8 MHz transmitter at Summit Station. Coaxial Times Microwave LMR-240 transmitted the antenna signal to the surface over 115 m of cable. Variations in the cable lengths led to sub-ns variation in arrival times between antenna channels.

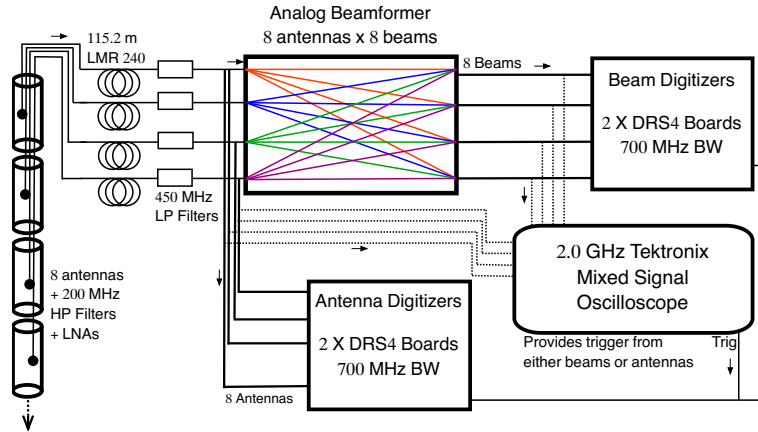


Figure 9. A schematic of the system deployed in Greenland. Only four signal chains and beam channels are shown for simplicity.

The signal from each antenna was split into two signal chain branches using 3 dB splitters. The first branch of the chain carried signals from individual antennas, while the second branch formed beams by splitting signals from each antenna eight ways, propagating signals from each antenna through fixed delay lines of Times Microwave LMR-200, and combining signals into eight beams at fixed angles from the horizontal. The system architecture allowed simultaneous digitization of both the antenna channels and the beams.

The instrument included up to eight broadband dipole antennas, described in Section 3.1.2. The number of antennas included in the array during the 2015 deployment season was tunable.

Waveforms from both branches of the signal chain (antenna channels and beam channels) were sampled at 2 GSa/s with record lengths of 1024 points with four DRS4 evaluation boards⁴. A Tektronix MSO5204B oscilloscope generated a global trigger for the digitizers using either automatic (unbiased) triggers or a threshold crossing on either an antenna or beam channel.

⁴<https://www.psi.ch/drs/evaluation-board>

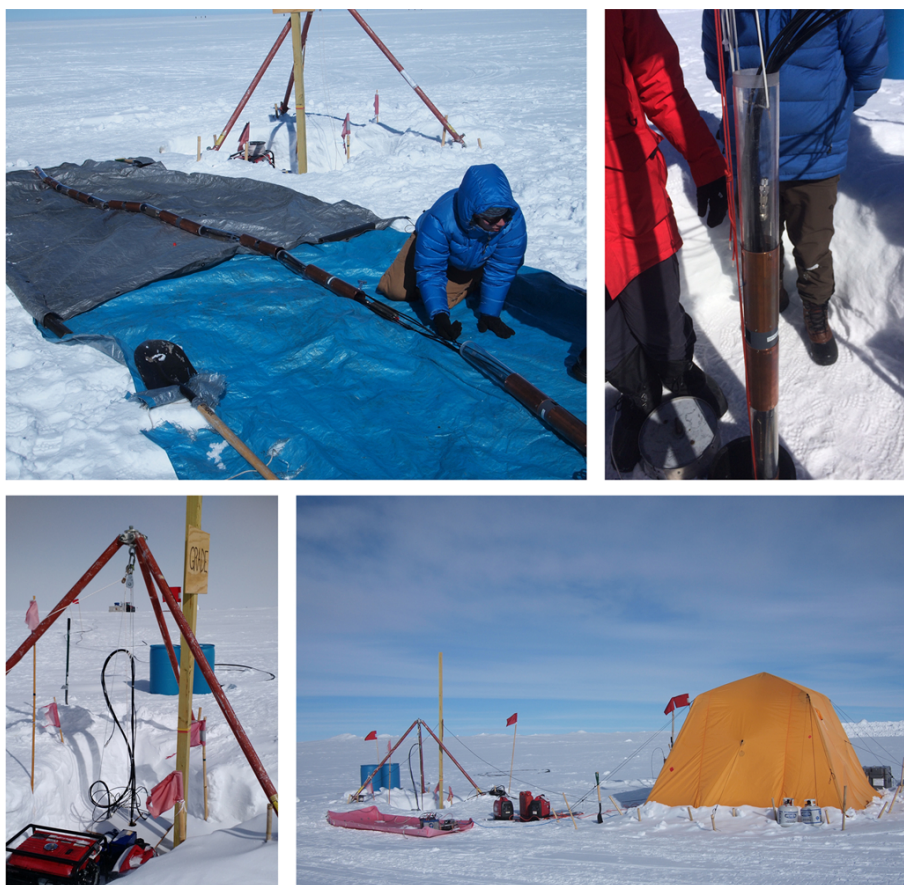


Figure 10. Pictures of the system deployment in Greenland. Upper left: laying out the antennas on the surface, before lowering the front-end system down the borehole. Upper right: lowering the antennas, amplifiers, and cabling down the borehole. Lower left: the system installed down the borehole. Lower right: the deployment camp, including deployment gantry and data-taking tent.

The eight antennas and front-end amplifiers were lowered down the DISC borehole⁵ using the gantry and winch system shown in Figure 10. The DISC borehole is located approximately 0.5 km from the main activities of the station. A fixed feed-to-feed antenna spacing of 76 cm was achieved using plastic spacers. Eight 115 m cables were bundled together at the surface of the ice and fed through the center of the topmost antennas and spacers such that signals from each individual antenna could be recorded. The bottom of the array was lowered to a depth of 96 m.

6.2 Noise Environment

During the June 2015 deployment, Summit Station was relatively radio quiet, with two notable exceptions. A balloon-borne radiosonde launched daily at Summit Station in support of the ICECAPS atmospheric monitoring program appears in our instrument at 402.8 MHz. The signal remains above thermal noise for several minutes, and the power falls off as the balloon

⁵<http://www.icedrill.org/equipment/disc.shtml>

drifts away. Transient signals at 150 MHz and 433 MHz also appear in the downhole antennas, due to station communications at those frequencies.

Figure 11 shows the power spectrum measured by a single downhole antenna. The power spectrum shown is the mean of 200 individual power spectra of 500-sample waveforms recorded on the oscilloscope, and is corrected for the overall gain in the signal chain. Uncertainties in the temperatures of the in-ice amplifiers and cables lead to a ± 3 dB uncertainty in the spectral power. As shown in the figure, noise observed on the downhole antenna is consistent with the expected thermal noise power in the 160-440 MHz band, defined by the 3 dB point of the filters used in the system, at 241 K, the temperature of the ice at 100 m depth [21].

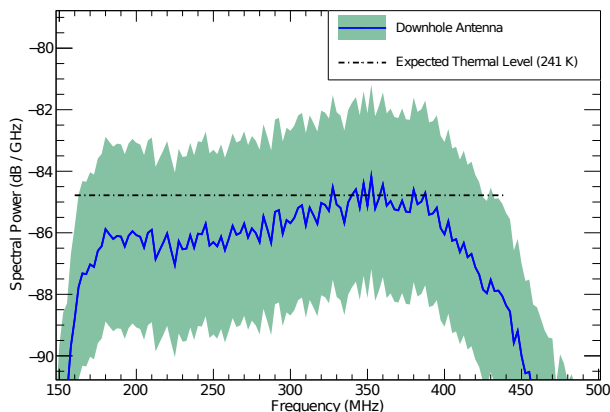


Figure 11. The average power spectral density for unbiased, thermal-noise triggers of a downhole antenna (blue solid line) compared with 241 K thermal noise (dashed line). A ± 3 dB error is shown, due to uncertainties in the temperatures of in-ice amplifiers and cables.

For uncorrelated noise, the RMS voltage in the beamformed channel, $V_{\text{RMS,beam}}$, is the quadrature sum of the RMS voltages, $V_{\text{RMS},i}$, in the individual antennas after accounting for the relative loss in the beamformer, L , which is -19.9 dB in power for the system deployed in Greenland. The loss in the beamformer is dominated by the 8-way splitter and 8-way combiner in each channel. Although digitizer noise is small ($< 2\%$ for beam channels and $< 0.5\%$ for antenna channels) compared to the system noise (thermal noise plus amplifier noise) level, we account for the RMS voltage from digitizer noise in both the antenna channels, $V_{\text{RMS}_{\text{D},i}}$, and the beam channel, $V_{\text{RMS}_{\text{D},\text{beam}}}$. The expected $V_{\text{RMS,beam}}$ is given by

$$V_{\text{RMS,beam}}^2 = 10^{L/10} \left(\sum_{\text{Nantennas}} (V_{\text{RMS},i}^2 - V_{\text{RMS}_{\text{D},i}}^2) \right) + V_{\text{RMS}_{\text{D},\text{beam}}}^2. \quad (6.1)$$

Figure 12 compares the expected to the measured $V_{\text{RMS,beam}}$ for five antennas combined using the analog beamformer. This data set consists of events recorded at a constant rate (unbiased) over the course of one night. A small fraction ($< 0.5\%$) of events that have high power in the 160-440 MHz band, indicative of man-made noise, are removed from the data set, leaving events dominated by thermal noise. The blue dashed line shows the expectation for an incoherent signal, such as thermal noise, while the red dashed line shows the expectation for a coherent signal, such as a true plane wave signal incident on the detector. The $< 10\%$ difference between the expected and measured $V_{\text{RMS,beam}}$ shows that the noise observed by

the downhole antennas adds incoherently when forming a beam, indicating that noise from adjacent in-ice antennas is uncorrelated. This is consistent with our results from anechoic chamber measurements (see Section 3.1).

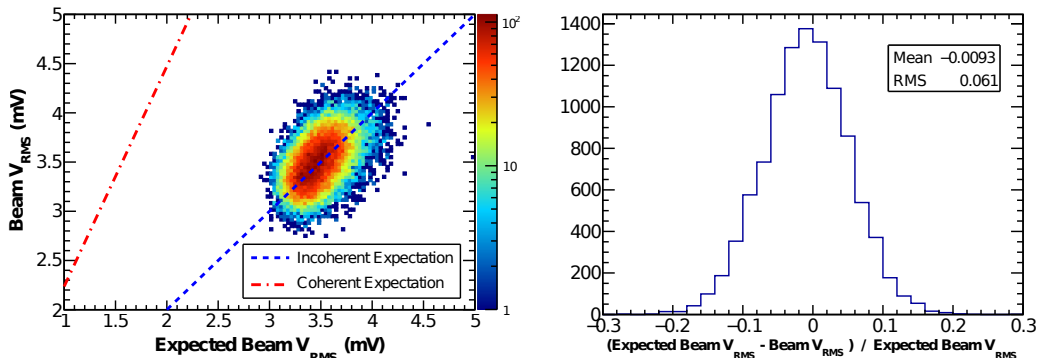


Figure 12. Expected V_{RMS} from a beam formed with five antennas compared to the measured V_{RMS} (left) and the fractional difference between the two (right).

6.3 Radio Attenuation Length of Ice at Summit Station

The depth-averaged field attenuation length at Summit Station has been measured to be $\langle L_\alpha \rangle = 947_{-85}^{+92}$ m at 75 MHz [22]. To directly compare this measurement with radio attenuation length measurements that have been made previously at other sites of developing and proposed neutrino detectors, such as the South Pole (the site of ARA) and Moore’s Bay on the Ross Ice Shelf (the site of ARIANNA), this measurement is extrapolated to 300 MHz and averaged over only the upper 1500 m of ice, which is where the interaction location would be for most neutrino events that are detectable by a surface or sub-surface detector. Assuming the measured temperature profile of ice at Summit Station and measured dependence of attenuation length on frequency, this indicates an average field attenuation length of 1022_{-253}^{+230} m over the upper 1500 m [22], compared to 1660_{-120}^{+255} m over the top 1500 m at 300 MHz at the South Pole [18] and 411 m with an experimental uncertainty of about 40 m averaged over all depths for the 578 m thick Moore’s Bay location [23, 24].

We can compare the electric field loss as a function of distance traveled through ice for the three candidate sites, which is the metric that is directly related to neutrino effective volume for a given detector. Figure 13 shows the electric field loss as a function of radio propagation distance through ice at candidate sites for neutrino detectors (Moore’s Bay, the South Pole, and Summit Station), including both the $1/r$ geometric factor and the measured attenuation length at each site. For neutrino events, which typically occur hundreds of meters from the detector, the loss seen through the ice at Summit Station is comparable to the loss seen through the ice at South Pole, and is much less than at Moore’s Bay.

6.4 Firn Properties at Summit Station

The slow transition from snow at the surface of the glacier to glacial ice in the bulk of the glacier is called the firn layer. This changing density over 100 m or more represents a changing index of refraction from that of snow near the surface ($n=1.35$) to that of ice below ($n=1.78$).

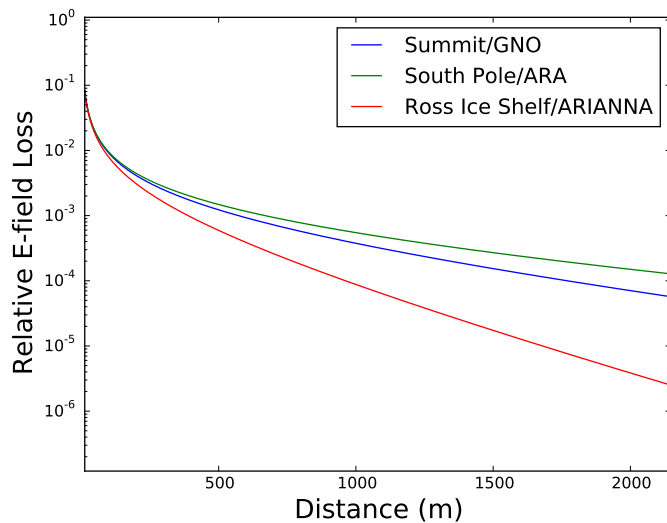


Figure 13. The electric field loss at 300 MHz as a function of radio propagation distance through ice at potential sites for neutrino detectors (Moore’s Bay, the South Pole, and Summit Station).

Radio signals emerging from the bulk ice below a surface or sub-surface detector must be able to refract through the firn and reach the detector in order for the instrument to trigger. This causes a shadowing effect, and the closer a detector is to the surface, the larger the wedge of volume located near the horizontal the detector cannot see (see for example Figure 7 in Reference [15]). Since radio emission from most neutrino events comes from near the horizontal, it is advantageous to deploy a detector below the firn layer at a given site [15].

At Summit Station, the density of the firn has reached 95% that of glacial ice by a depth of 100 m [25]. At the South Pole, the density has reached 95% that of glacial ice by a depth of 140 m [26]. Therefore, a detector deployed below the surface at Summit Station would require shallower drilling compared to the South Pole.

7 Conclusions

The in-ice phased array for detection of high-energy neutrinos is a promising technique. We have performed studies that demonstrate that thermal noise is uncorrelated between tightly-packed neighboring antennas in each other’s nulls. We have also validated the beamforming technique through simulations and measurements in an anechoic chamber, achieving the expected improvement in SNR when beamforming using an experimental system. We have also built and deployed a phased array in-ice for testing at Summit Station in Greenland and have measured the noise environment at Summit Station.

A simulation including realistic parameters for an FPGA-based correlation trigger indicates that phasing signals from multiple low-gain antennas yields significant improvement in achieved trigger threshold, consistent with idealized expectations and anechoic chamber measurements. We are designing and constructing such a trigger to be implemented first at the South Pole on the ARA experiment. Pending successful demonstration of the technique, a larger array with hundreds of antennas per station could be proposed either at the South Pole

or in Greenland to achieve a low energy threshold capable of providing significant overlap in energy with IceCube in the PeV energy range, and extending the measurement of high energy neutrinos through the higher-energy cosmogenic neutrino range.

Acknowledgments

We would like to thank CH2M Hill and the US National Science Foundation (NSF) for the dedicated, knowledgeable, and extremely helpful logistical support team enabling us to perform our work at Summit Station, particularly to J. Jenkins. We are deeply indebted to those who dedicate their careers to help make our science possible in such remote environments. We would like to thank the University of Wisconsin-Madison IceCube and ARA groups for allowing us to use their anechoic chamber and the ARA collaboration for lending the ARA bicone and slot antennas for testing. We also thank D. Arakaki for the use of anechoic chambers at the California Polytechnic State University for antenna characterization measurements. This work was supported by the Kavli Institute for Cosmological Physics at the University of Chicago, Department of Energy Grant DE-SC0009937, and the Leverhulme Trust. Computing resources were provided by the University of Chicago Research Computing Center.

References

- [1] IceCube Collaboration, M. G. Aartsen, et al., *Observation of High-Energy Astrophysical Neutrinos in Three Years of IceCube Data*, *Phys. Rev. Lett.* **113** (Sept., 2014) 101101.
- [2] IceCube Collaboration, M. G. Aartsen, et al., *First Observation of PeV-Energy Neutrinos with IceCube*, *Phys. Rev. Lett.* **111** (July, 2013) 021103.
- [3] IceCube Collaboration, M. G. Aartsen, et al., *A combined maximum-likelihood analysis of the high-energy astrophysical neutrino flux measured with IceCube*, *Astrophys. J.* **809** (2015), no. 1 98.
- [4] K. Greisen, *End to the Cosmic-Ray Spectrum?*, *Phys. Rev. Lett.* **16** (Apr., 1966) 748–750.
- [5] G. T. Zatsepin and V. A. Kuz'min, *Upper Limit of the Spectrum of Cosmic Rays*, *JETP Letters* **4** (Aug., 1966) 78.
- [6] V. S. Beresinsky and G. T. Zatsepin, *Cosmic rays at ultra high energies (neutrino?)*, *Physics Letters B* **28** (Jan., 1969) 423–424.
- [7] G. Askaryan, *Excess Negative Charge of an Electron-Photon Shower and its Coherent Radio Emission*, *Soviet Physics JETP* **14** (2) (1962) 441–443.
- [8] ANITA Collaboration, P. W. Gorham, et al., *Observations of the Askaryan Effect in Ice*, *Phys. Rev. Lett.* **99** (Oct., 2007) 171101.
- [9] P. W. Gorham et al., *Accelerator measurements of the Askaryan effect in rock salt: A roadmap toward teraton underground neutrino detectors*, *Phys. Rev. D* **72** (July, 2005) 023002.
- [10] D. Saltzberg et al., *Observation of the Askaryan Effect: Coherent Microwave Cherenkov Emission from Charge Asymmetry in High-Energy Particle Cascades*, *Phys. Rev. Lett.* **86** (Mar., 2001) 2802.
- [11] ANITA Collaboration, P. W. Gorham, et al., *Observational constraints on the ultrahigh energy cosmic neutrino flux from the second flight of the ANITA experiment*, *Phys. Rev. D* **82** (July, 2010) 022004.
- [12] P. W. Gorham et al., *The ExaVolt Antenna: A large-aperture, balloon-embedded antenna for ultra-high energy particle detection*, *Astroparticle Physics* **35** (Dec., 2011) 242–256.

- [13] ARA Collaboration, P. Allison, et al., *Performance of two Askaryan Radio Array stations and first results in the search for ultrahigh energy neutrinos*, *Phys. Rev.* **D93** (2016), no. 8 082003.
- [14] S. W. Barwick et al., *A first search for cosmogenic neutrinos with the ARIANNA Hexagonal Radio Array*, *Astroparticle Physics* **70** (Oct., 2015) 12–26.
- [15] A. G. Vieregge, K. Bechtol, and A. Romero-Wolf, *A technique for detection of PeV neutrinos using a phased radio array*, *J. Cosm. and Astropart. Phys.* **2** (Feb., 2016) 005.
- [16] IceCube Collaboration, S. Schoenen, L. Radel, et al., *A measurement of the diffuse astrophysical muon neutrino flux using multiple years of icecube data*, *Proc. of Science ICRC2015* (2015) 1179, [[arXiv:1510.05223](https://arxiv.org/abs/1510.05223)].
- [17] K. Kotera, D. Allard, and A. V. Olinto, *Cosmogenic neutrinos: parameter space and detectability from PeV to ZeV*, *J. Cosm. and Astropart. Phys.* **10** (Oct., 2010) 13.
- [18] ARA Collaboration, P. Allison, et al., *Design and initial performance of the Askaryan Radio Array prototype EeV neutrino detector at the South Pole*, *Astroparticle Physics* **35** (Feb., 2012) 457–477.
- [19] J. W. Goodman, *Statistical Optics, 2nd Ed.* John Wiley and Sons, Inc., 2015.
- [20] S. Wissel et al., *Site characterization and detector development for the greenland neutrino observatory*, *Proc. of Science ICRC2015* (2015) 1150.
- [21] Greenland Ice Core Project, <ftp://ftp.ncdc.noaa.gov/pub/data/paleo/icecore/greenland/summit/grip/physical/griptemp.txt>, 1994.
- [22] J. Avva et al., *An in situ measurement of the radio-frequency attenuation in ice at Summit Station, Greenland*, *J. Glaciol.* **61** (2015) 1005–1011.
- [23] T. Barrella, S. Barwick, and D. Saltzberg, *Ross Ice Shelf (Antarctica) in situ radio-frequency attenuation*, *J. Glaciol.* **57** (Mar., 2011) 61–66.
- [24] J. C. Hanson et al., *Radar absorption, basal reflection, thickness, and polarization measurements from the Ross Ice Shelf, Antarctica*, *J. Glaciol.* **61** (2015), no. 227.
- [25] R. B. Alley and B. R. Koci, *Ice-Core Analysis at Site A, Greenland: Preliminary Results*, *Annals of Glaciology* **10** (1988).
- [26] Koci and Kuivinen, *A 237-meter ice core from South Pole Station*, *Antarctic Journal of the U.S.* **18** (1983), no. 5 113–114.